



ΠΑΝΕΠΙΣΤΗΜΙΟ ΚΡΗΤΗΣ - ΤΜΗΜΑ ΕΦΑΡΜΟΣΜΕΝΩΝ ΜΑΘΗΜΑΤΙΚΩΝ  
Archimedes Center for Modeling, Analysis & Computation  
UNIVERSITY OF CRETE - DEPARTMENT OF APPLIED MATHEMATICS  
Archimedes Center for Modeling, Analysis & Computation



## ACMAC's PrePrint Repository

### **Application of inverse Abel techniques in in-line holographic microscopy**

*Michael Apostolopoulos and Michael Taroudakis and Dimitrios Papazoglou*

#### *Original Citation:*

Apostolopoulos, Michael and Taroudakis, Michael and Papazoglou, Dimitrios  
(2013)

*Application of inverse Abel techniques in in-line holographic microscopy.*

Optics Communications, Elsevier.

ISSN 0030-4018

(In Press)

This version is available at: <http://preprints.acmac.uoc.gr/195/>

Available in ACMAC's PrePrint Repository: March 2013

ACMAC's PrePrint Repository aim is to enable open access to the scholarly output of ACMAC.

<http://preprints.acmac.uoc.gr/>

# Application of inverse Abel techniques in in-line holographic microscopy

M. I. Apostolopoulos<sup>a,\*</sup>, M. I. Taroudakis<sup>b, c</sup> and D.G. Papazoglou<sup>d, e, §</sup>

- <sup>a</sup> *Department of Applied Mathematics, University of Crete, Knossou Ave, 71409, Heraklion, Greece.*
- <sup>b</sup> *Institute of Applied and Computational Mathematics, Foundation for Research and Technology-Hellas, N. Plastira 100, 71110 Heraklion, Greece.*
- <sup>c</sup> *Department of Mathematics, University of Crete, Knossou Ave, 71409, Heraklion, Greece.*
- <sup>d</sup> *Institute of Electronic Structure and Laser, Foundation for Research and Technology-Hellas, N. Plastira 100, 71110 Heraklion, Greece.*
- <sup>e</sup> *Materials Science and Technology Department, University of Crete, P.O. Box 2208, 71003 Heraklion, Greece.*

\* Corresponding author,

E-mail address: [mapostol@tem.uoc.gr](mailto:mapostol@tem.uoc.gr) (M. I. Apostolopoulos), [dpapa@materials.uoc.gr](mailto:dpapa@materials.uoc.gr)

**Abstract:** In this paper, we compare two well established techniques, namely the BASEX and the Fourier - Hankel, as regards their efficiency of retrieving the three-dimensional distribution of cylindrically symmetric objects in the presence of noise. This situation is commonly encountered in pump-probe experiments where the refractive index profile of elongated structures, such as plasma strings or transient refractive index changes, is under study. We performed numerical experiments for a variety of objects, with respect to the spatial distribution and size, and for various statistical distributions and

M. I. Apostolopoulos, M. I. Taroudakis and D. G. Papazoglou

levels of noise. In this area of application, the BASEX can surpass the Fourier Hankel technique in respect of reconstruction quality, spatial resolution and robustness to noise especially after proper tuning of the basis set functions width.

**Keywords:** Inhomogeneous optical media, Image reconstruction techniques, Inverse problems, Microscopy.

## 1. Introduction

In the field of holographic microscopy [1-6], the treatment of inverse problems, as for instance, that of recovering the volume of the three-dimensional distribution of the refractive index, is based on the application of various techniques of Abel transform. The Abel transform [7-9] is actually a solution of the inverse mathematical problem of retrieving the three-dimensional distribution of a physical property such as the refractive index or absorption on the basis of the knowledge of a single projection. This problem is ill posed [9], as we cannot prove that a unique solution exists, unless the distribution is spherically or axially symmetric, in which case, the inverse Abel transform, provides a unique solution.

In the field of image analysis, the forward Abel transform is used in order to project, an axially symmetric distribution function, onto a plane. In this respect, the measured intensity (projection),  $P(x, z)$ , is given in terms of the distribution function  $R(r, z)$ , via the Abel transform [7-9] as follows :

$$P(x, z) = 2 \int_x^{\infty} \frac{R(r, z)r}{(r^2 - x^2)^{1/2}} dr, \quad (1)$$

where  $r$  is the radial coordinate, with  $r^2 = x^2 + y^2$  and  $x$  is the coordinate along the projection. A geometric interpretation of the Abel transform is depicted in Fig. 1. In this figure, a ray propagating

1 M. I. Apostolopoulos, M. I. Taroudakis and D. G. Papazoglou

2  
3 parallel to the  $y$ -axis passes through a circularly symmetric object (indicated by blue color) and reaches  
4  
5 the observer located at  $(O)$ . If the circularly symmetric function  $R(r, z)$  denotes the distribution of  
6  
7 absorption for this object then the total absorption experienced by the ray is given by the Abel transform  
8  
9 described in eq. (1).  
10  
11  
12  
13

14 In many cases, the projection function  $P(x, z)$  is measured, while the distribution function  $R(r, z)$ , is  
15  
16 unknown. The solution of this inverse problem is performed by means of the inverse Abel transform [9]:  
17  
18  
19

$$20 \quad R(r, z) = -\frac{1}{\pi} \int_r^{\infty} \frac{(\partial P / \partial x)}{(x^2 - r^2)^{1/2}} dx \quad (2)$$

21  
22  
23

24 Practically, the numerical implementation of equation (2) is difficult due to the singularity point at the  
25  
26 lower limit of integral and because the derivative of the projection  $(\partial P / \partial x)$  tends to enhance the noise-  
27  
28 corruption of the experimental data. Moreover, the projection function  $P(x, z)$ , cannot be treated as a  
29  
30 continuous function, as its value is known only in certain discrete points [9]. Various approaches that are  
31  
32 based on geometrical or numerical methods and on the use of polynomials, have been adopted aiming at  
33  
34 the calculation of the inverse Abel transform [9-15].  
35  
36  
37  
38

39 It should be noted, that an extension of this inverse problem to a truly three dimensional distribution may  
40  
41 be treated using the inverse Radon transform [16]. Taking into account that the two-dimensional Radon  
42  
43 transform is defined as the projection of a physical property along a specific radial direction [16], the  
44  
45 retrieval of a three-dimensional object's structure involves the inverse Radon transform of a number of its  
46  
47 projections. This approach is widely applied in tomographic imaging applications where the object under  
48  
49 study is somewhat static. On the other hand, it is quite difficult to retrieve the large number of projections  
50  
51 required in the case of dynamical objects encountered in ultrafast pump-probe experiments [1-6]. In this  
52  
53 case the objects under study are laser induced perturbations in the refractive index of a transparent  
54  
55 medium with micron sized spatial dimensions. Furthermore, these structures dynamically change with  
56  
57 time at time scales well below 1 ps. All the above mentioned problems make the retrieval from multiple  
58  
59  
60  
61  
62  
63  
64  
65

1 M. I. Apostolopoulos, M. I. Taroudakis and D. G. Papazoglou

2  
3  
4 projections impractical, leading to the utilization of a single projection and an implementation of the Abel  
5  
6 transform for the retrieval of the refractive index distribution [2, 6].  
7

8  
9 Up to now, the commonly applied method for calculating the inverse Abel transform in problems of laser  
10  
11 induced perturbations is the Fourier–Hankel technique (F-H) [2, 6, 9]. More specifically, this method is  
12  
13 based on a representation of the inverse Abel transform (eq. (2)) via the Hankel transform of the Fourier  
14  
15 transform of the measured projection [9]. In this scheme, the distribution  $R(r, z)$ , can be calculated from  
16  
17 the measured projection  $P(x, z)$  via the following expression,  
18  
19  
20  
21

$$22 \quad R(r, z) = 2\pi \int_0^\infty q J_0(2\pi kr) \int_{-\infty}^\infty P(x, z) \exp(-i2\pi xk) dx dk \quad (3)$$

23  
24  
25

26 where,  $J_0(\cdot)$  is the zero-order Bessel function of the first kind [17]. For an axial symmetric object  
27  
28 extending along the  $z$  axis (Fig. 1) this procedure is iterated for each  $z$  in order to obtain the distribution  
29  
30 along  $z$ . However, this method is sensitive to experimental noise, especially of high spatial frequency. In  
31  
32 order to eliminate the effect of noise low pass filtering [2, 6] is used. This approach has though a  
33  
34 deteriorating effect in extremely noisy images as well as to images with a large dynamic range [18] where  
35  
36 the filtering can affect the fine details of the reconstructed object.  
37  
38  
39

40  
41 The Gaussian basis-set expansion Abel transform method, also called as BASEX method, is a recently  
42  
43 developed method of reconstructing three-dimensional images from their two-dimensional projections  
44  
45 [18]. This method is based on expanding the projection in a basis set of functions that are analytical  
46  
47 projections of known well-behaved functions. The three-dimensional distribution can then be  
48  
49 reconstructed as a linear combination of these functions, which have a Gaussian-like shape, with the same  
50  
51 expansion coefficients as the projection [18]. At this point, it should be noted, that BASEX method is up  
52  
53 to now mainly applied, with great success, to two-dimensional projections of three-dimensional spherical  
54  
55 objects encountered in photoelectron imaging spectroscopy.  
56  
57  
58  
59  
60  
61  
62  
63  
64  
65

In this work we compare the BASEX and the F-H methods by using them to retrieve the distribution of three-dimensional objects with cylindrical symmetry from two-dimensional projections that are commonly encountered in pump-probe experiments [2-6]. In particular we numerically study the effect of noise on the reconstruction results for various typical distributions. Our results show that especially after an optimization process, regarding the width of the basis functions, the BASEX technique can eventually outperform the F-H technique with better reconstruction quality and less sensitivity to noise.

This paper is organized as follows: In Section 2 we present a direct adaptation of the BASEX method to cylindrically symmetric objects. In section 3 we illustrate extensive numerical simulations and assess the behavior and effectiveness for both BASEX and F-H techniques after applying them to noisy distributions. We end with a summary and conclusions in section 4.

## 2. Adaptation of the BASEX method in cylindrical objects

Since the BASEX method has been analytically developed and detailed described for spherical objects [18, 19], we need to adapt it to the simpler case of cylindrical objects. The approach is quite straightforward, but for the sake of completeness, we will repeat the basic elements of the method, the details of which can be found in [18, 19]. For cylindrically symmetric distributions  $R(r, z)$ , where  $z$  is the axis of symmetry, the distribution can be expanded, following the BASEX method via a set of  $K$  basis radial functions  $\rho_k(r)$ , as following:

$$R(r, z) = \sum_{k=0}^{K-1} C_k^f(z) \rho_k(r) \quad (4)$$

where  $C_k^f(z)$  are expansion coefficients, which in our case depend on  $z$ . In view of this, the projection  $P(x, z)$  of the distribution function  $R(r, z)$  along the  $x$ - $z$  plane (Fig. 1), given in (2), can be similarly expanded as

M. I. Apostolopoulos, M. I. Taroudakis and D. G. Papazoglou

$$P(x, z) = \sum_{k=0}^{K-1} C_k(z) G_k(x) \quad (5)$$

where,

$$G_k(x) = 2 \int_x^{\infty} \frac{\rho_k(r) r}{(r^2 - x^2)^{1/2}} dr, \quad k = 0, \dots, K-1 \quad (6)$$

are the projections of the basis functions  $\rho_k(r)$  after applying forward Abel transform and the  $C_k(z)$  are expansion coefficients to be calculated.

Furthermore, since the projection  $P(x, z)$  is retrieved using discrete devices like CCD cameras, equation (5) can be rewritten in a discrete form for a  $N_x \times N_z$  pixels projection image, as follows:

$$P_{ij}^{(K)} = \sum_{k=0}^{K-1} C_k(z_j) G_i^{(k)}, \quad (7a)$$

where,

$$G_i^{(k)} = 2 \int_{x_i}^{\infty} \frac{\rho_k(r) r}{(r^2 - x_i^2)^{1/2}} dr, \quad i = 1, \dots, N_x \text{ and } j = 1, \dots, N_z \quad (7b)$$

Eq. (7a) can be solved independently for each  $z_j$ . In this case for a single  $z_j$  it is written in matrix form as

$$\mathbf{P} = \mathbf{C} \mathbf{G} \quad (8)$$

which is a system of equations representing the inverse problem in two dimensions. Here,  $\mathbf{C}$  and  $\mathbf{G}$  are vectors

$$\mathbf{C} = (\mathbf{C}^{(0)}, \dots, \mathbf{C}^{(K-1)}), \quad \mathbf{G} = (\mathbf{G}^{(0)}, \dots, \mathbf{G}^{(K-1)})^T, \quad \{\mathbf{C}^{(k)}, \mathbf{G}^{(k)} \in \mathbf{R}^K\}.$$

As it was shown in [18] an appropriate set of basis functions  $\rho_k(r)$  is given by the relation

$$\rho_k(r) = \exp[-2(\frac{r}{\sigma} - k)^2], \quad k = 0, \dots, K-1 \quad (9)$$

where  $\sigma$  is a parameter related to the width of Gaussian base functions  $\rho_k(r)$  and  $K \leq (N_x + 1)/2$ . These Gaussian base functions represent a good basis set due to the analytical expression of their Abel inversion [19] and are used in all cases analyzed later on, in this paper. The term  $K$  depends both on the corresponding width of the projection image and the selection width parameter  $\sigma$  of the Gaussian basis functions. For instance, to adequately cover the object area, the selection of a narrow basis functions with  $\sigma = 1$  requires that  $K = N_x / 2$ , while if  $\sigma = 2$ ,  $K = N_x / 4$ . Recall that we are interested in recovering cylindrical density distributions. The system (8) yields the corresponding expansion coefficients by solving the least-squares problem via the Tikhonov regularization which is used in order to ensure the stability on an ill-posed problem giving ultimately accurate approximate solutions [18, 20]:

$$\mathbf{C} = \mathbf{P}\mathbf{G}^T (\mathbf{G}\mathbf{G}^T + q_x^2 \mathbf{I})^{-1}, \quad q_x > 0 \quad (10)$$

where  $\mathbf{I}$  is the identity matrix and  $q_x^2$  is the regularization parameter of  $G_i^{(k)}$  for the  $x$  dimension. The process of regularization is utilized aiming at the improvement of the condition number of the matrix  $\mathbf{G}\mathbf{G}^T$  [21-24] which is equal to the ratio of the highest ( $\sigma_{\max}(\mathbf{G}\mathbf{G}^T)$ ) to the lowest ( $\sigma_{\min}(\mathbf{G}\mathbf{G}^T)$ ) singular value [24-26] of matrix  $\mathbf{G}\mathbf{G}^T$  and is expressed by the following relation,

$$Cond(\mathbf{G}\mathbf{G}^T) = \|\mathbf{G}\mathbf{G}^T\|_2 \cdot \|(\mathbf{G}\mathbf{G}^T)^{-1}\|_2 = \frac{\sigma_{\max}(\mathbf{G}\mathbf{G}^T)}{\sigma_{\min}(\mathbf{G}\mathbf{G}^T)} \geq 1 \quad (11)$$

The regularization parameter  $q_x^2$  is a positive and free parameter that enters into the final solution of eq. (10) and affects the amount of noise suppression in the two-dimensional reconstructed distribution projection. Very small values of the parameter should be avoided due to the appearance of high frequency noise in the reconstruction [20, 22, 23]. Likewise, very large values should also be avoided because they lead to information loss in the reconstruction [20, 22, 23]. The determination of the optimal Tikhonov



regularization factor  $q_x^2$  has been achieved, in all numerical results below, by following an approach relying on the Bayesian interpretation, taking into account all the crucial assumptions arising from this method [27].

### 3. Simulated objects

To study the efficiency of each of the two methods on analyzing two-dimensional projections of cylindrically symmetric objects we have first simulated two conically shaped objects. Although the specific objects are not commonly encountered in experiments there are interesting to study numerically since their width is monotonically varied enabling to examine the effect of object size on the reconstruction. The radial distribution function of the first one, referred from now on as *Reference Object 1*, is shown in Fig. 2(a) (in normalized units). As it is clear from the figure the object is conical in shape with gradually increasing width and smooth edges. The radial distribution function of the second one, referred from now on as *Reference Object 2*, is shown in Fig. 2(b) (in normalized units). The radial distribution function of this object is described by a Super Gaussian distribution. In both cases the distribution functions might refer to the perturbation of the refractive index, induced by a strong ultrafast pulse. In Fig. 2(c) a radial profile of the normalized density distribution is shown for both objects. The analytical expressions that describe the density distribution of these objects are:

$$R_1(r, z) = \exp\left[-4 \ln 2 \frac{r^2}{w(z)^2}\right] \quad (12)$$

$$R_2(r, z) = \exp\left[-2^{2n} \ln 2 \frac{r^{2n}}{w(z)^{2n}}\right] \quad (13)$$

where  $w(z) = z$  and  $n = 8$ . The two dimensional projections of these objects were calculated numerically by using the direct Abel transform of eq. (1) and are shown in Figs. 3(a) and 3(b)

respectively. These projections correspond to the measurable quantity in any experimental configuration. Therefore, in order to study the effect of noise on the reconstruction we numerically generated noisy projections by adding different levels noise in the original projections. This approach closely mimics the real experiments where noise is emerging during the projection retrieval.

In experiments noise can originate from inhomogeneities of the probe beam spatial distribution (speckle, interference fringes etc.) or from the detection device (CCD sensor). The statistical properties of noise differ depending on its source. Noise originating from the CCD sensor can be adequately described by white Gaussian noise. On the other hand, probe beam inhomogeneities exhibit more complex statistical properties, which are related to the experimental setup used. In order to cover the widest possible noise statistical scenarios we have used both the generic distribution of white Gaussian noise and also noise with statistical properties retrieved from a series of experimental images.

Typical images of noisy projections, using white Gaussian noise, are shown in Figs. 3(c) and 3(d). The noise in these images corresponds to typical noise levels encountered in real experiments. Normally a single number describing the ratio of the signal to noise (SNR) would suffice to describe the strength of noise in a projection. In our case the situation is more complicated since both objects, have variable width while the RMS noise amplitude is constant over the whole projection. As shown in Fig. 3(e), the SNR ratio depends on the width (FWHM) of the object and roughly stabilizes to a saturation value for large widths. The Noise Level 2, for instance, corresponds to noise level of the power of  $SNR = 13 \pm 2dB$ , approximately. This behavior is also repeated in the case of *Reference Object 2* (not shown here).

Next, we compared the two methods BASEX and F-H by applying them to the reconstruction of the simulated objects shown in Fig. 2 using as an input their noisy projections (shown in Fig. 3). In the case of the BASEX technique we utilized two different sets of basis functions: **(a)**.  $K = 100$ ,  $\sigma = 1$ ,  $q_x^2 = 15$  and **(b)**.  $K = 50$ ,  $\sigma = 2$ ,  $q_x^2 = 28$ , respectively. On the other hand, in the case of the F-H technique, we used low pass Gaussian filtering to reduce the effect of noise in the reconstruction. In this case the Fourier

transform of the projection ( $P(x,z)$  in eq. (3)) first multiplied by a Gaussian function before the Hankel transform was applied [9]. The amount of low pass filtering was adjusted by changing the width of the Gaussian filter function, a process which effectively equivalent to the numerical aperture ( $NA$ ) of an optical system. We applied two different levels of filtering : **(i)** weak filtering referring to  $NA = 0.85$ , and **(ii)**. strong filtering referring to  $NA = 0.17$ . Fig. 4, shows the reconstruction results for the *Reference Object 1* and at Noise Level 1 ( $SNR = 33 \pm 2dB$ ), Noise Level 2 ( $SNR = 13 \pm 2dB$ ) and Noise Level 3 ( $SNR = 3 \pm 2dB$ ). It is clear that both methods, qualitatively at least, sufficiently reconstruct the original objects for the first two noise levels where noise is not that strong. On the other hand, the F-H technique, as shown in Figs 4(f) and 4(e), seems to be more robust to high levels of noise compared to BASEX. One reason behind this is the low pass filtering that is used in the F-H technique. The results for the case of *Reference Object 2* (not shown here), are similar.

For better understanding the effect of each reconstruction method in Fig. 5 we show typical line profiles of the original and reconstructed objects for  $SNR = 13 \pm 2dB$  noise level. For the BASEX technique results from both sets ( $\sigma = 1, 2$ ) of basis functions are shown, while for the F-H technique two low pass filtering levels (*weak* (i) and *strong* (ii)) are applied. These results quantitatively confirm the qualitative result of Fig. 4, that for such type of objects the F-H technique leads to a more accurate reconstruction compared to the BASEX. The low pass filtering plays a very important role here since for weaker filtering F-H results in quite noisy reconstructions. Besides the object reconstruction the baseline (zero in our case) is well recovered in the F-H reconstructions compared to the BASEX. On the other hand, the BASEX technique is more robust to the effect of noise as the basis set becomes wider. This is an expected result since wider base functions filter out noise components that correspond to higher spatial frequency practically acting like a low pass filter.

The dependence of the RMS reconstruction error on the typical size (FWHM) of the object for various noise levels is shown in Fig. 6. For the BASEX technique the wider ( $\sigma = 2$ ) basis set is used while for the F-H the stronger low pass filtering is applied. It is clear that for this type of objects the F-H results

systematically to a lower RMS error compared to BASEX. On the other hand, the F-H shows some sensitivity on the size of the reconstructed object since the RMS error ( $0.0210 \pm 0.0182$ ) can vary by an order of magnitude (Fig. 6 (a)) as the object size changes while, on the contrary, the BASEX shows a much lower variation of the RMS reconstruction error ( $0.0557 \pm 0.0038$ ). This effect is weakened as the noise level is increasing but still the F-H shows a stronger variation as a function of the object size. The BASEX technique although is in general less robust in noise for the types of objects and noise used, it exhibits remarkable stability as the object size varies. So in this respect it is superior compared to F-H since the RMS reconstruction error will be independent of the original object size.

It is expected that the increase of the width of the Gaussian functions of the BASEX basis set will further reduce the effect of noise on the reconstruction. In this sense the BASEX technique can be better adapted for the reconstruction of noisy projections. As shown in Fig. 7(a) the RMS error for a noisy projection ( $SNR = 13 \pm 2dB$ ) is monotonically decreased as the basis set width is increased. On the other hand, simply measuring the global RMS error in a reconstruction can be misleading. As also shown in Fig. 7(a) if we focus only on small features (with typical feature size  $w < 12$  in our simulations) the reconstruction fails to be accurate even in the absence of noise. Clearly in this case the increase of the basis set width leads to loss of resolution. In order to optimize the BASEX technique the two opposing trends of sensitivity to noise and resolution should be balanced. This, as shown in Fig. 7(a), is achieved at a basis set width of  $\sigma \sim 3.5 \pm 0.5$  roughly 3.5 times smaller than the width of the typical feature size. Using this optimization process we obtain a roughly threefold reduction of the RMS reconstruction error in presence of noise.

In order to confirm this significant argument, in Fig. 7(b) we illustrate typical line profiles of fine structured objects (where typical feature size  $w < 12$ ) for the case of *Reference Object 1* and the corresponding reconstructed objects at Noise Level 2. To do so, the optimum F-H technique (*strong* (ii)) is applied, while the optimized BASEX for a set of basis functions where  $\sigma = 3.7$ , is presented. After inspecting the plots in Fig. 7(b), we conclude that after this optimization process the BASEX technique

M. I. Apostolopoulos, M. I. Taroudakis and D. G. Papazoglou

can clearly provide more reliable results compared to the F-H. Thus, after appropriately tuning the basis set functions width, the BASEX approach is better than F-H in all aspects.

The study of conically shaped objects (*Reference obj. 1 and 2*), although not commonly encountered in pump-probe experiments, has provided us with valuable information regarding the effect of object size on the reconstruction and enabled us to finely tune the BASEX basis set.

We now extend our study to three commonly encountered types of cylindrical reference objects. In all cases the distribution functions again refer to the perturbation of the refractive index, typically induced by a strong ultrafast pulse in the experiments. The radial distribution function of the first one, referred from now on as *Reference Object 3*, is shown in Fig. 8(a) (in normalized units) and is described by the analytical expression:

$$R_3(r, z) = \exp[-4 \ln 2 \left( \frac{z-z_o}{w_z} \right)^2 \left( \frac{r}{w_o} \right)^2] \quad (14)$$

where  $z_o = 25$  is the peak position along  $z$ ,  $w_z = 30$  and  $w_o = 18$  are respectively the FWHM of the distribution along  $z$  axis (at  $r = 0$ ) and along  $r$  (at  $z = z_o$ ). The radial distribution function of the second one, referred from now on as *Reference Object 4*, is shown in Fig. 8(b) (in normalized units) and is described by a Gaussian distribution sinusoidally modulated along  $z$  axis:

$$R_4(r, z) = \{1 + m \cdot \cos[\frac{2\pi}{\Lambda}(z - \frac{z_o}{6})]\} \exp[-4 \ln 2 \left( \frac{z-z_o}{w_z} \right)^{2\mu} \left( \frac{r}{w_o} \right)^2] \quad (15)$$

where  $z_o = 25$ ,  $\mu = 2$ ,  $w_z = 30$ ,  $w_o = 25$  refer to the spatial characteristics of the Gaussian envelope function and,  $\Lambda = 20$ ,  $m = 0.8$  refer to the modulation period and strength. This distribution mimics generation of plasma hotspots during the dynamic propagation, along the propagation axis  $z$ , of an intense beam in the non-linear propagation regime [2, 5, 6]. The radial distribution function of the third one,

M. I. Apostolopoulos, M. I. Taroudakis and D. G. Papazoglou

referred from now on as *Reference Object 5*, is shown in Fig. 8(c) (in normalized units) and is described by the analytical expression:

$$R_5(r, z) = \frac{w_0^2}{w_0^2 + (z - z_o)^2} \exp[-4 \ln 2 \left( \frac{r}{w_0} \right)^2] \quad (16)$$

where  $z_o = 25$ ,  $w_0 = 16$  refer respectively to the peak position along  $z$  and the FWHM of the distribution along  $r$  (at  $z = z_o$ ). This kind of distribution mimics the typical focusing of a Gaussian pump beam with a Gaussian transverse distribution (along  $r$ ) and a Lorentzian distribution along  $z$ . In Figs. 8(d), 8(e) and 8(f), the two dimensional projections of these objects, which were numerically generated by applying the direct Abel transform of eq. (1), are illustrated. Note again, that these projections correspond to the measurable quantity of interest in any experiment.

In the following, we compared the optimized BASEX ( $\sigma=3.7$ ) and F-H ( $NA = 0.17$ ) techniques by applying them to noisy projections of *Reference Objects* 3,4 and 5, using again white Gaussian noise. Fig. 9, shows the comparative reconstruction results for the *Reference Object 3* (Fig.9-top row), the *Reference Object 4* (Fig.9-middle row) and the *Reference Object 5* (Fig. 9-bottom row) at Noise Level 2, and for both reconstruction methods. More precisely, the typical image of noisy projection ( $SNR = 13 \pm 2dB$ ) of the *Reference Object 3* is shown in Fig. 9-top left. On the center and right plots the results for both the optimized BASEX and the optimum F-H techniques are depicted, correspondingly. In the middle and bottom rows of the same figure the corresponding results for the *Reference Object 4* and the *Reference Object 5*, respectively, are illustrated. It is clear that both optimal methods, qualitatively at least, provide quite satisfactory retrievals of the original cylindrical objects, with a lower loss of resolution for the optimized BASEX compared to the optimum F-H. We also observe that for the first two types of cylindrical objects the optimum F-H technique, leads to a slightly more accurate reconstruction with respect to the optimized BASEX method. In particular, the RMS reconstruction error for the F-H ranges from 0.0294 (*Reference obj. 3*) to 0.0259 (*Reference obj. 4*), while for the Basex method varies from

M. I. Apostolopoulos, M. I. Taroudakis and D. G. Papazoglou

0.0351 (*Reference obj. 3*) to 0.0467 (*Reference obj. 4*), respectively. On the contrary, for the *Reference Object 5*, the optimized Basex shows a slightly lower RMS reconstruction error (RMS = 0.0308) compared to the F-H technique (RMS = 0.0316). This behavior of the F-H technique is due to dependence of the reconstruction quality on the initial object size. On the other hand, the Basex's reconstruction quality is practically independent to the object size. Moreover, our simulations (not shown here) for this type of objects systematically result to a lower RMS error for the optimized BASEX (RMS = 0.0308) compared to the narrow BASEX basis set Gaussian functions ( $\sigma \leq 2$ ) (RMS = 0.0722).

Up to now we have limited our study on the effect of white Gaussian noise on the reconstructions which adequately describes noise originating from the CCD sensor but is not efficient in describing noise originating from probe beam inhomogeneities. In order to extend our study to the effect of noise closer resembling the experiment we have first analyzed the statistical properties of noise using a collection of 120 experimental images. The spatial spectral distribution of noise in each image was retrieved, as a function of the spatial frequency, by radially averaging its Fourier transform. The statistical distribution of the whole image collection was then obtained by averaging the individual radial spectral distributions. The Fig. 10 depicts the normalized spatial spectral distribution of the whole image set as a function of the spatial frequency. The experimental points are well fitted by a Gaussian envelope function:

$$S(f) = p_o + (1 - p_o) \text{Exp}[-4 \ln 2 (f/f_w)^2] \quad (17)$$

where  $f$  is the spatial frequency (in  $\text{pixels}^{-1}$ ),  $p_o \cong 0.18$  represents a white noise background and  $f_w \cong 0.1 \text{ pixel}^{-1}$  is the spectral FWHM of the Gaussian distribution. In comparison the spectral distribution of an averaged set of simulated white Gaussian noise is also shown in Fig. 10. Although due to the normalization process the two distributions look quite different it is clear that above a spatial frequency of  $f > 0.2 \text{ pixel}^{-1}$  (corresponding to intensity variations with a periodicity less than 5 pixels) the noise distribution is practically white.

We have numerically generated realistic noise images by using the spatial spectral distribution described in Eq. (17) as a spatial spectrum envelope function to white Gaussian noise. This approach enables us to obtain a random noise with the desired statistics. To implement this numerically a pseudo random complex numbers array  $a + i\beta$  is firstly generated, and since  $\alpha$  and  $\beta$  are independent and random their variation conforms to the normal distribution with mean value zero and standard deviation 1. This array, that corresponds to the spatial Fourier transform of the required random noise distribution, is then multiplied by the envelope function  $S(f)$ , where  $f$  is the spatial frequency. By inverse Fourier transforming this shaped random spectral distribution  $(a + i\beta) \cdot S(f)$  we retrieve the desired random noise field  $n_1 + in_2$ . Finally, since the noise will be applied to the intensity values of each projection, only the real part is used in the simulations. Typical noise images resulting from this approach are shown in Fig. 11. The images in Fig. 11 are generated using different spectral FWHM values ranging from values similar to the experimental images Fig. 11(a) to values practically leading to white Gaussian noise.

We further compared the optimized BASEX ( $\sigma = 3.7$ ) and the optimum F-H ( $NA = 0.17$ ) methods by applying them to noisy projections of *Reference Object 5*, adding simulated noise with statistical properties similar to the experimental images as depicted in Fig. 11(a). The Signal to Noise ratio (SNR) was adjusted by properly scaling the noise amplitude values. Fig. 12, illustrates the comparative results for the *Reference Object 5* adding experimental noise at different typical SNR values for both reconstruction techniques. On the left column of Fig. 12, the typical images of noisy projections (SNR = 33dB, 13dB and 3dB respectively) of the *Reference Object 5*, are shown. On the center and right columns, the reconstruction results for the optimized Basex and the optimum F-H methods are presented, respectively, for each typical noise level. It is clear that both techniques are successfully reconstructing the initial objects even for high noise levels. Interestingly, these results are comparable to the reconstruction results obtained using white Gaussian noise. More precisely the RMS reconstruction error for the Basex technique ranges at 0.0338 while the F-H results in 0.0334 values, at SNR = 13dB. For the case of *Reference Objects 3* and *4* (not shown here) we get similar results. More specifically, the RMS



1 M. I. Apostolopoulos, M. I. Taroudakis and D. G. Papazoglou

2  
3 error for the Basex ranges from 0.0381 (*Reference obj. 3*) to 0.0445 (*Reference obj. 4*), while for the F-H  
4  
5 technique varies from 0.0323 (*Reference obj. 3*) to 0.0277 (*Reference obj. 4*), correspondingly, at the  
6  
7 same SNR level.  
8  
9

10  
11 To further explore the effect of noise statistical distribution we preformed reconstructions using noisy  
12  
13 projections varying the noise statistics while keeping the SNR constant. The simulations were preformed  
14  
15 adding the noise distributions depicted in Fig. 11 to the projection of *Reference Object 5*. In all cases the  
16  
17 noise values were properly scaled so that the SNR is 13 dB. In Fig. 13, are shown the comparative results  
18  
19 for the BASEX and the F-H techniques. Note, that the noise distributions are indexed from 1 to 4,  
20  
21 corresponding to Fig. 11(a), 11(b), 11(c), and 11(d) respectively. On the left column of Fig. 13, we show  
22  
23 the respective projections with the addition of noise (SNR = 13dB). On the center and right columns, the  
24  
25 reconstruction results for the optimized Basex and the optimum F-H methods are presented, respectively.  
26  
27 It is clear that both techniques, even for a wide range of noise statistical distributions, reconstruct quite  
28  
29 sufficiently the initial object. This confirms the validity of the results obtained using white Gaussian  
30  
31 noise, since both reconstruction techniques are not sensitive to the noise statistics in the parameters range  
32  
33 that was examined. The RMS reconstruction error for the Basex technique ranges from 0.0261 (noise  
34  
35 screen 1) to 0.0298 (noise screen 4), while the F-H results from 0.0226 (noise screen 1) to 0.0259 (noise  
36  
37 screen 4) values, respectively. In this case the optimized F -H technique, seems to provide, quantitatively  
38  
39 at least, a slightly more accurate reconstruction compared to the optimized BASEX method. Furthermore,  
40  
41 our simulations (not shown here) for this wide range of noise statistical distributions result to a lower  
42  
43 RMS error for the optimized BASEX (RMS =0.0347) compared to the narrow BASEX basis set Gaussian  
44  
45 functions ( $\sigma \leq 2$ ) (RMS =0.0689), as for instance, at noise screen 2. This behavior is also repeated in the  
46  
47 cases of *Reference Objects 3* and *4* (not shown here). More concretely, the RMS reconstruction error for  
48  
49 the optimized BASEX ranges from 0.0398 (*Reference obj. 3*) to 0.0504 (*Reference obj. 4*), while for the  
50  
51 narrow BASEX basis set varies from 0.0694 (*Reference obj. 3*) to 0.0652 (*Reference obj. 4*), respectively,  
52  
53 at the same noise screen.  
54  
55  
56  
57  
58  
59  
60  
61  
62  
63  
64  
65

Overall, we conclude, that the BASEX method can be better adapted for the reconstruction of noisy projections compared to the F-H, especially after appropriately optimizing the basis set Gaussian functions width. A further advantage of the BASEX technique compared to the F-H concerns the amount of processing power. For typical reconstructions like the ones presented in this paper, the BASEX technique is approximately 15 times faster, and 1000 times faster in the calculation of the inverse Abel transform needed to derive the matrix of the expansion coefficients, described in equation (10). This aspect should be seriously taken into account in cases where a real time reconstruction is required.

#### 4. Summary and conclusions

In this paper we compared two widely used reconstruction techniques for the reconstruction of cylindrical objects typically encountered in laser pump-probe experiments, namely the BASEX technique, appropriately adapted to the reconstruction of cylindrical objects, and the F-H technique. Our numerical experiments were performed for a variety of objects, with respect to the spatial distribution and size, and for various noise levels and statistical distributions. The noise level and distribution was selected to cover a wide range corresponding to noise encountered in typical pump-probe experiments.

Analyzing the numerical experiments, it is clearly shown that for such noisy projections a straightforward application of the BASEX technique, using a narrow Gaussian basis set, results to a slightly worse reconstruction quality compared to the low pass filtered F-H technique. On the other hand, by widening the base functions used in the BASEX technique the reconstruction becomes less sensitive to noise with the drawback of reducing the spatial resolution. We also show that the BASEX technique can be optimized for noisy projections by adapting the basis set width to be approximately 3-4 times smaller than the typical feature size.

Another important aspect is the dependence of the reconstruction quality on the original object size. The low pass filtering used in the F-H technique results to a strong dependence of the reconstruction

1 M. I. Apostolopoulos, M. I. Taroudakis and D. G. Papazoglou  
2  
3

4 quality on the object size. Thus, small objects are not well recovered by the F-H technique. This is not a  
5  
6 problem for the BASEX technique, where the reconstruction quality is practically independent of the  
7  
8 object size. Finally the F-H technique is by at least 15 times more computationally intensive than the  
9  
10 BASEX.  
11  
12

13  
14 Furthermore, we confirmed that both techniques are robust to variations of the noise statistics. Using a  
15  
16 collection of experimental images we have retrieved the typical statistical noise distribution for this  
17  
18 application which we then exploited to generate simulated noise with the desired statistics. Our results  
19  
20 show that both reconstruction techniques exhibit similar behavior in respect noise with statistical  
21  
22 properties ranging from white Gaussian noise to typical experimental one.  
23  
24

25  
26 In summary, for typical cylindrical objects encountered in pump-probe holographic interferometry  
27  
28 experiments, the BASEX is superior to the F-H method especially after proper optimization of the basis  
29  
30 set functions width.  
31  
32  
33  
34  
35  
36  
37  
38  
39  
40  
41  
42  
43  
44  
45  
46  
47  
48  
49  
50  
51  
52  
53  
54  
55  
56  
57  
58  
59  
60  
61  
62  
63  
64  
65

1 M. I. Apostolopoulos, M. I. Taroudakis and D. G. Papazoglou  
2  
3

#### 4 **References**

5  
6 [1] D. G. Papazoglou, I. Zergioti, S. Tzortzakis, Optics Letters 32 (2007) 2055-2057.  
7

8  
9 [2] D. G. Papazoglou and S. Tzortzakis, Applied Physics Letters 93 (2008) 041120.  
10

11  
12 [3] S. Minardi, A. Gopal, M. Tatarakis, A. Couairon, G. Tamosauskas, R. Piskarskas, A. Dubietis, and P.  
13 Di Trapani, Opt. Lett. 33 (2008) 86.  
14

15  
16 [4] G. Rodriguez, A. R. Valenzuela, B. Yellampalle, M. J. Schmitt, and K.-Y. Kim, J. Opt. Soc. Am. B 25  
17 (2008) 1988.  
18

19  
20 [5] S. Minardi, A. Gopal, A. Couairon, G. Tamoasuskas, R. Piskarskas, A. Dubietis, and P. Di Trapani,  
21 Opt. Lett. 34 (2009) 3020.  
22

23  
24 [6] D. Abdollahpour, D. G. Papazoglou, and S. Tzortzakis, Phys. Rev. A 84 (2011) 053809.  
25

26  
27 [7] R. N. Bracewell, The Fourier Transform and its Applications, third ed., McGraw-Hill, New York,  
28 2000.  
29

30  
31 [8] H. R. Griem, Plasma Spectroscopy, McGraw-Hill, New York, 1964.  
32

33  
34 [9] L. Montgomery Smith, Dennis R. Keefer, S. I. Sudharsanan, J. Quant. Spectrosc. Radiat. Transfer 39  
35 (1988) 367-373.  
36

37  
38 [10] O. H. Nestor and H. N. Olsen, SIAM Rev. 22 (1960) 200-207.  
39

40  
41 [11] K. Bockasten, J. Opt. Soc. Am. 51 (1961) 943-947.  
42

43  
44 [12] M. J. Freeman and D. Katz, J. Opt. Soc. Am. 53 (1963) 1172-1179.  
45

46  
47 [13] C. J. Cremers and R. C. Birkebak, Appl. Opt. 5 (1966) 1057-1063.  
48

49  
50 [14] C. D. Maldonado, A. P. Caron, H. N. Olsen, J. Opt. Soc. Am. 55 (1965) 1247-1251.  
51  
52  
53  
54  
55  
56  
57  
58  
59  
60  
61  
62  
63  
64  
65

1 M. I. Apostolopoulos, M. I. Taroudakis and D. G. Papazoglou  
2  
3

4 [15] Pablo A. Vicharelli, Walter P. Lapatovich, Appl. Phys. Lett. 50 (1987) 557-559.  
5  
6

7 [16] S. G. Gindikin, Mh. Math. 113 (1992) 23-32.  
8  
9

10  
11 [17] G. N. Watson, A treatise on the Theory of Bessel Functions, second ed., Cambridge University Press,  
12 1966.  
13  
14

15  
16 [18] V. Dribinski, A. Ossadtchi, V. A. Mandelshtam, H. Reisler, Rev. Sci. Instrum., 73 (2002) 2634-  
17 2642.  
18  
19

20  
21 [19] K. R. Overstreet, P. Zabawa, J. Tallant, A. Schwettmann and J. P. Shaffer, Optics Express 13 (2005)  
22 9672-9682.  
23  
24

25  
26 [20] A. N. Tikhonov, Sov. Math. Dokl. 4, (1963) 1035-1038.  
27  
28

29  
30 [21] L. N. Trefethen, D. Bau, Numerical linear Algebra, SIAM, Philadelphia, PA, 1997.  
31  
32

33  
34 [22] E. W. Cheney, D. R. Kincaid, Numerical Mathematics and Computing, sixth ed., Brooks/Cole,  
35 Monterey CA, 2007, p. 321.  
36  
37

38  
39 [23] G. H. Golub and C. F. Van Loan, Matrix Computations, third ed., John Hopkins University Press,  
40 1996.  
41  
42

43  
44 [24] M. Marcus and H. Minc, Introduction to Linear Algebra, New York: Dover, 1988, p. 191.  
45  
46

47  
48 [25] M. Marcus and H. Minc, A Survey of Matrix Theory and Matrix Inequalities, New York: Dover,  
49 1992, p. 69.  
50  
51

52  
53 [26] E. T. Whittaker and G. N. Watson, A course in Modern Analysis, fourth ed., Cambridge, England:  
54 Cambridge University Press, 1990, pp. 524-528.  
55  
56  
57  
58  
59  
60  
61  
62  
63  
64  
65

1 M. I. Apostolopoulos, M. I. Taroudakis and D. G. Papazoglou  
2  
3

4 [27] Jaynes, E.T., Bayesian Methods: General Background, in Maximum-Entropy and Bayesian Methods  
5  
6 in Applied Statistics, in J. H. Justice (ed.), Cambridge, UK: Cambridge University. Press, 1986, p. 1.  
7  
8  
9  
10  
11  
12  
13  
14  
15  
16  
17  
18  
19  
20  
21  
22  
23  
24  
25  
26  
27  
28  
29  
30  
31  
32  
33  
34  
35  
36  
37  
38  
39  
40  
41  
42  
43  
44  
45  
46  
47  
48  
49  
50  
51  
52  
53  
54  
55  
56  
57  
58  
59  
60  
61  
62  
63  
64  
65

## List of Figure Captions

Fig. 1. (Color online) A geometrical interpretation of the Abel transform of a cylindrically symmetric function  $R(r, z)$ . An observer ( $O$ ) looks along a line parallel to the  $y$  axis, a distance  $x$  above the origin. He sees the projection  $P(x, z)$  of the circularly symmetric function along the line of sight. Inset: Detail at a cross sectional  $x$ - $y$  plane.

Fig. 2. (Color online) The synthetic-simulated images of initial conical reference objects called as (a). Gauss-Filled-Cone (*Reference Object 1*) and (b). Top-Hat-Filled-Cone (*Reference Object 2*), respectively. (c). The imaging of general distribution of the radial profiles of two reference objects.

Fig. 3. (Color online) The 2D projections of the initial conical (a). *Reference Object 1* and (b). *Reference Object 2*, respectively, after using forward Abel transform. The corresponding noisy projections of (c). *Reference Object 1* and (d). *Reference Object 2*, while adding white Gaussian noise (Noise Level 2). (e). The graphical representation of SNR (dB) with respect to the FWHM (*pixels*) in several noise levels for the *Reference Object 1*. The dotted black line indicates the threshold of noise which is of power of SNR = 3dB.

Fig. 4. (Color online) **Left column:** The reconstructing results obtained through Basex ( $\sigma = 2$ ) for the *Reference Object 1* at (a). Noise Level 1, (c). Noise Level 2 and (e). Noise Level 3, respectively. **Right column:** The retrieving results provided via F-H by using a strong low pass Gaussian filtering (NA=0.17), at (b). Noise Level 1, (d). Noise Level 2 and (f). Noise Level 3, correspondingly. The reconstructed objects obtained by both methods are represented in an optimal color scale locked at [-1.2, 1.2] interval.

Fig. 5. (Color online) The graphical representation of variation for the profile (in a central line) of reconstructed *Reference Object 1*, after using (a). Basex in two different basis functions ( $\sigma = 1, 2$ ) and (b). F-H in two different filtering levels (*weak* (i) and *strong* (ii)), respectively, at Noise Level 2. The

graphical representation of variation for the profile (in a central line) of reconstructed *Reference Object 2*, after applying (c). Basex in two different basis functions and (d). F-H in two different filtering levels (*weak* (i) and *strong* (ii)), correspondingly, at the same Noise Level. The black line indicates the distribution of profiles for the reference objects, in the same central line.

Fig. 6. (Color online) **Left column:** The RMS-error results provided through both reconstruction techniques with respect to the FWHM (*pixels*) for the *Reference Object 1* at (a). Noise Level 1, (b). Noise Level 2 and (c). Noise Level 3. **Right column:** The RMS-error results provided through both reconstruction techniques with respect to the FWHM (*pixels*) for the *Reference Object 2* at (d). Noise Level 1, (e). Noise Level 2 and (f). Noise Level 3, respectively. The green line represents the RMS-error results by using the Basex ( $\sigma = 2$ ) method and the red one indicates the RMS-error results after applying F-H method in appropriate filtering level (*strong case*, (ii)).

Fig. 7. (Color online) (a). RMS-error of the Basex method as a function of the Gaussian basis function width. (■) Global RMS error in the presence of noise, (●) mean RMS error for the reconstruction of small objects (widths  $< 12$ ) in the absence of noise. (The dashed and dotted lines are guides to the eye). (b). The graphical representation of variation for the profile (in a line where typical feature size  $w < 12$ ) of reconstructed *Reference Object 1*, after using (a). the optimized Basex ( $\sigma = 3.7$ ) and (b). the optimum F-H (*strong* (ii)), respectively, at Noise Level 2. The black line indicates the distribution of the profile of the reference object.

Fig. 8. (Color online) Simulated typical cylindrical reference objects (a). Double Gauss (*Reference Object 3*), (b). Modulated Double Gauss (*Reference Object 4*) and (c). Typical Focus (*Reference Object 5*). The corresponding 2D projections of (d). *Reference Object 3*, (e). *Reference Object 4* and (f). *Reference Object 5*, after applying forward Abel transform.



M. I. Apostolopoulos, M. I. Taroudakis and D. G. Papazoglou

Fig. 9. (Color online) Noisy projections (noise Level 2) and the corresponding reconstruction results obtained using the optimized Basex ( $\sigma=3.7$ ) and F-H ( $NA = 0.17$ ) techniques. **Top row:** *Reference Object 3*. **Middle row** *Reference Object 4*. **Bottom row:** *Reference Object 5*.

Fig. 10. (Color online) Normalized spatial spectral noise distribution as a function of the spatial frequency (in  $\text{pixels}^{-1}$ ). (●) Spatial spectra retrieved from 120 images experimental images, (gray line) Gaussian fit, (blue line) simulated white Gaussian noise.

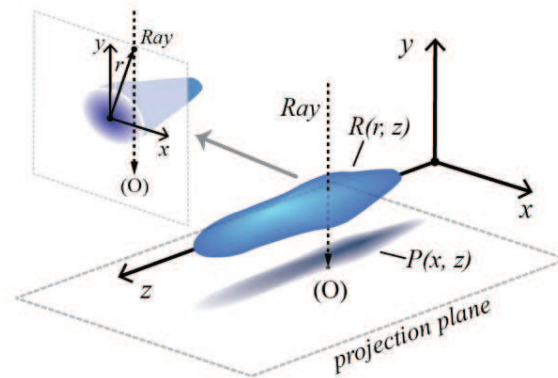
Fig. 11. (Color online) Typical noise images generated using random spectral phase distribution shaped by a Gaussian envelope function as described in Eq. (17) **(a).**  $f_w = 0.1 \text{ pixel}^{-1}$  (similar to typical experimental noise), **(b).**  $f_w = 0.36 \text{ pixel}^{-1}$ , **(c).**  $f_w = 0.77 \text{ pixel}^{-1}$ , and **(d).**  $f_w = 1 \text{ pixel}^{-1}$  (similar to white Gaussian Noise). In all cases the background white value is set to  $p_o = 0.18$

Fig. 12. (Color online) Effect of noise, with statistical distribution similar to the experiment, for various SNR levels. **Left column:** The 2D noisy projections of *Reference Object 5* while adding noise at different SNR levels (33dB, 13dB, 3dB). **Center column:** Reconstruction results after applying the optimized Basex ( $\sigma = 3.7$ ). **Right column:** Reconstruction results after using the optimum F-H ( $NA = 0.17$ )

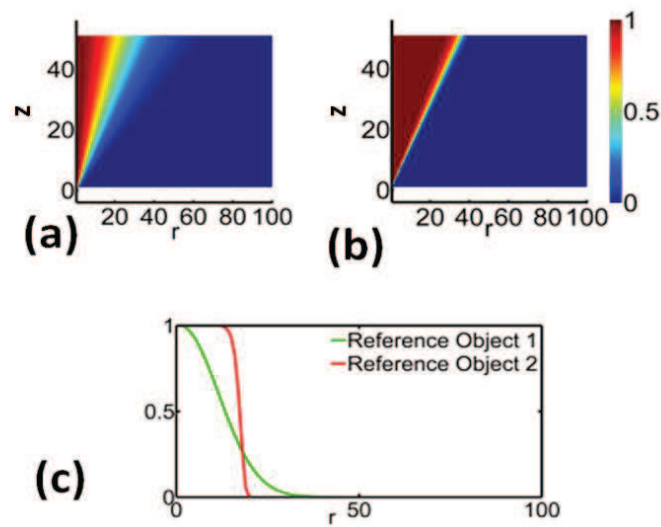
Fig. 13. (Color online) Effect of the statistical distribution of noise in the reconstruction at a constant SNR=13 dB level. **Left column:** The 2D noisy projections of *Reference Object 5* while consecutively adding noise with varying statistical properties corresponding to Fig. 11. **Center column:** Reconstruction results after applying the optimized Basex ( $\sigma = 3.7$ ). **Right column:** Reconstruction results after using the optimum F-H ( $NA = 0.17$ ).

## Figures

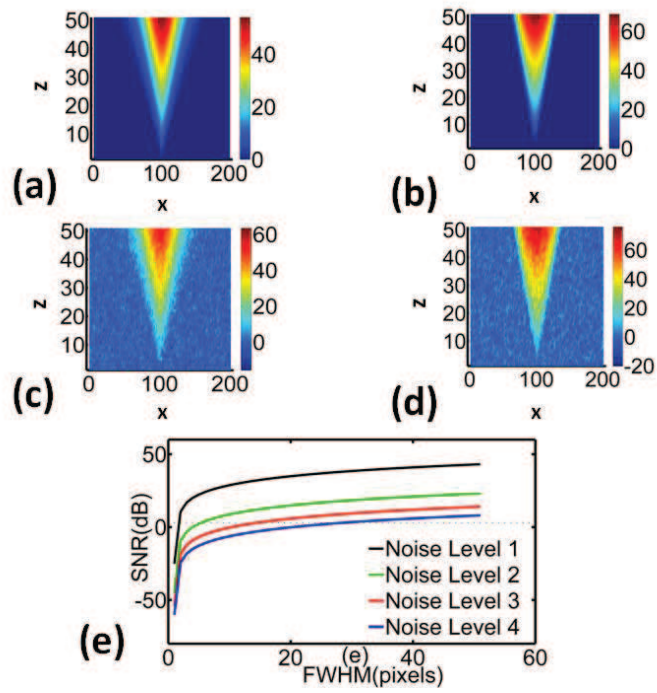
1.



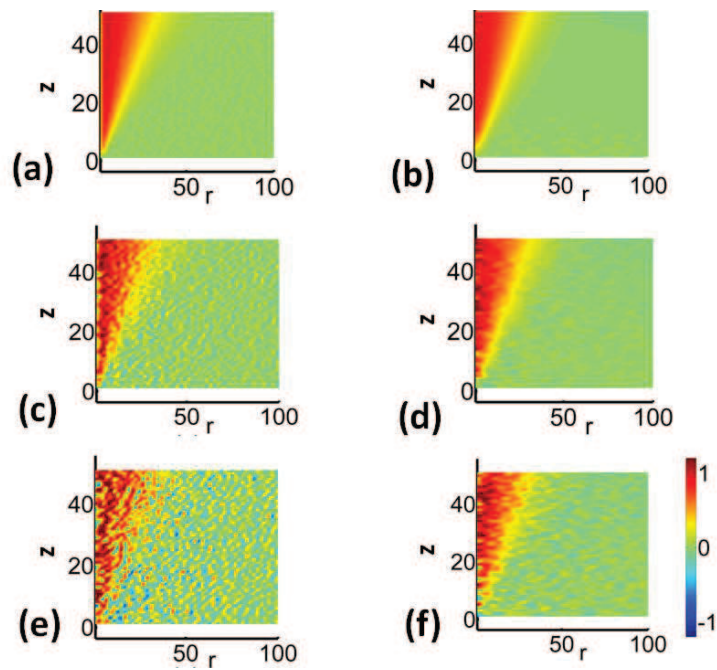
2.



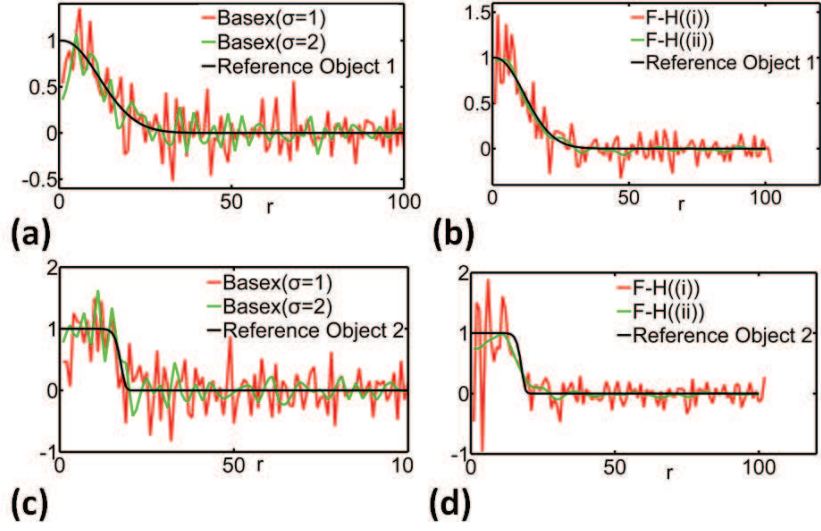
3.



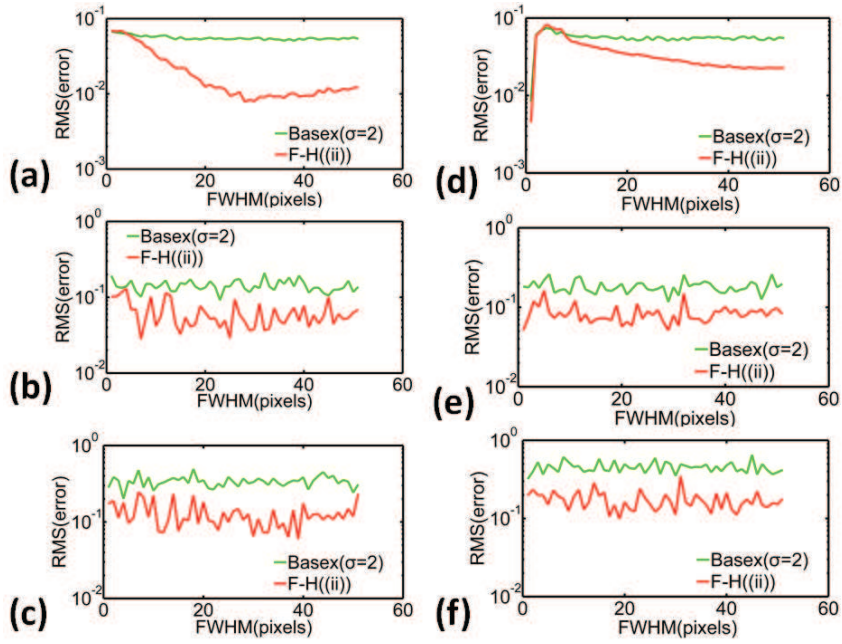
4.



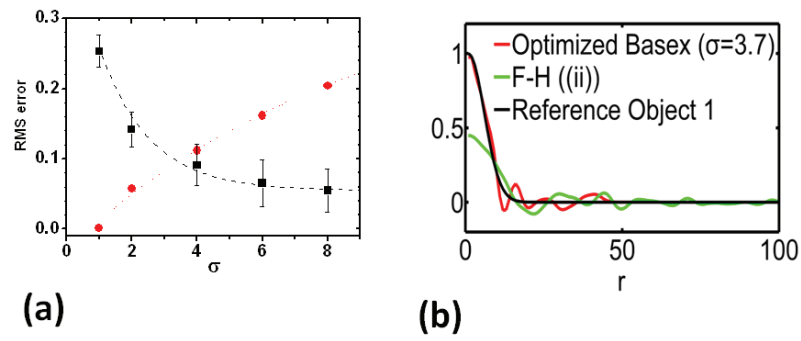
5.



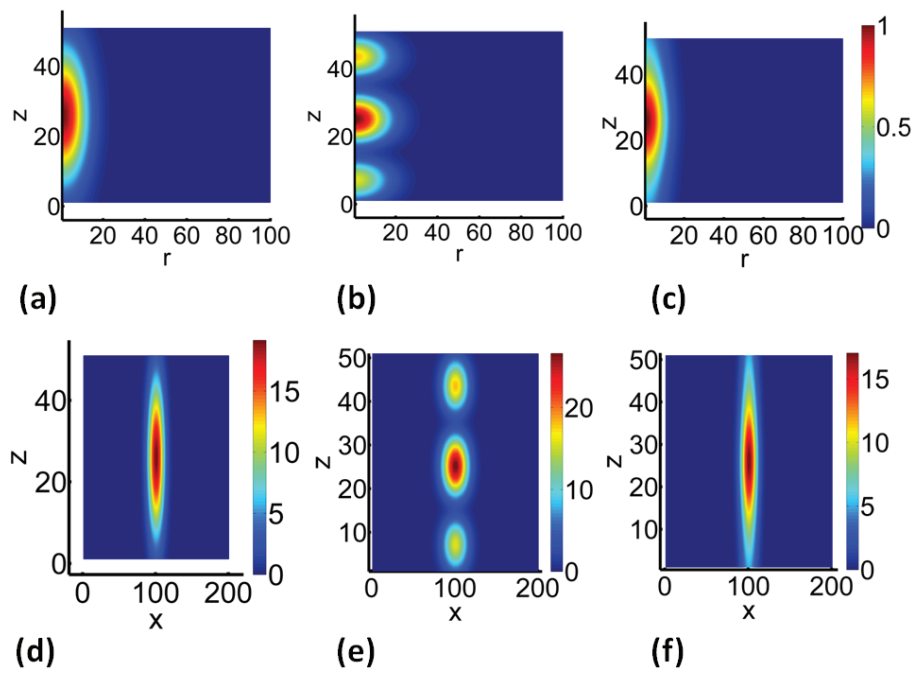
6.



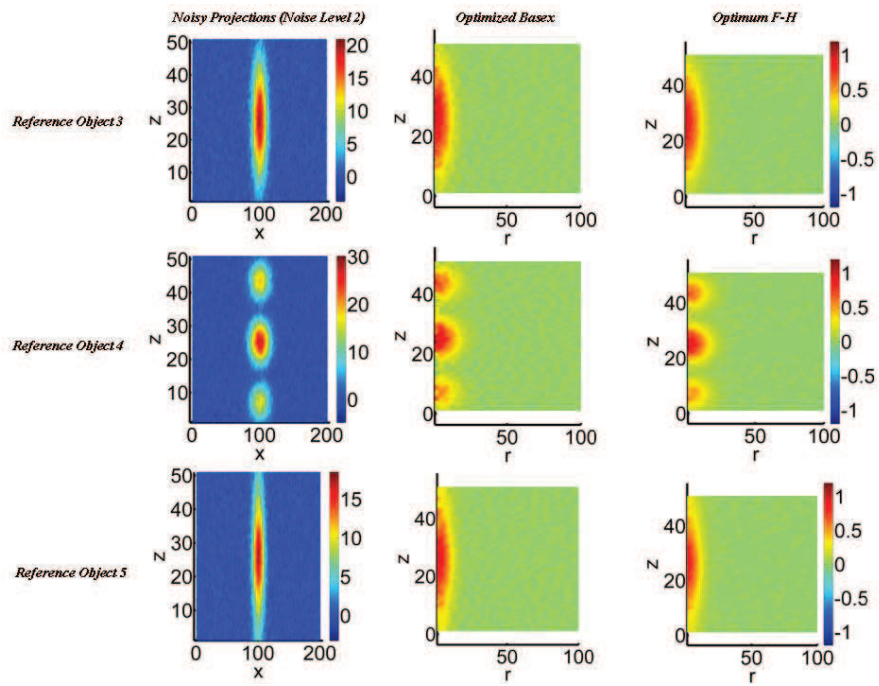
7.



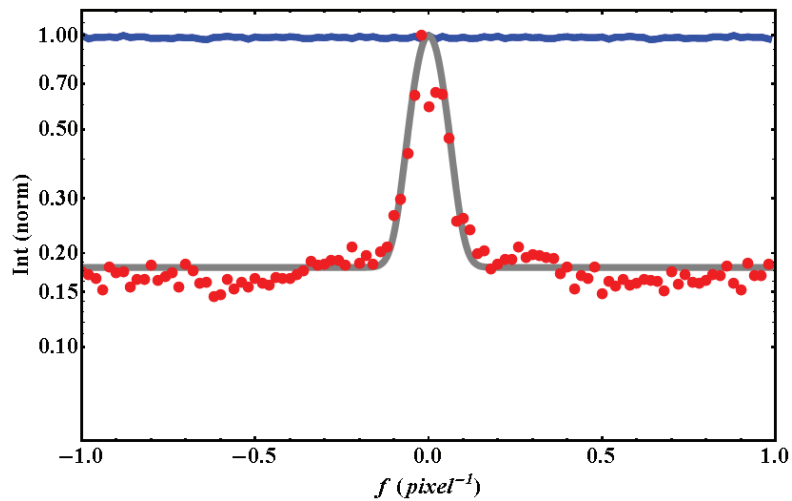
8.



9.

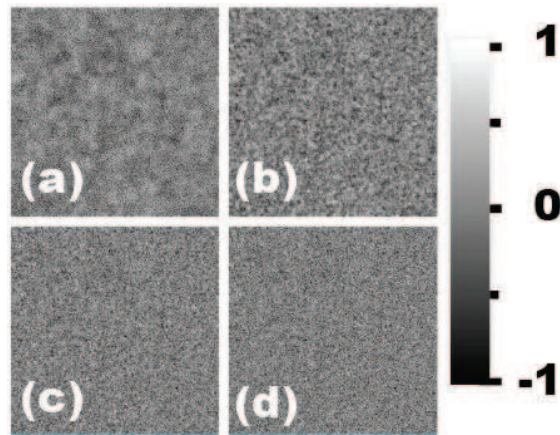


10.

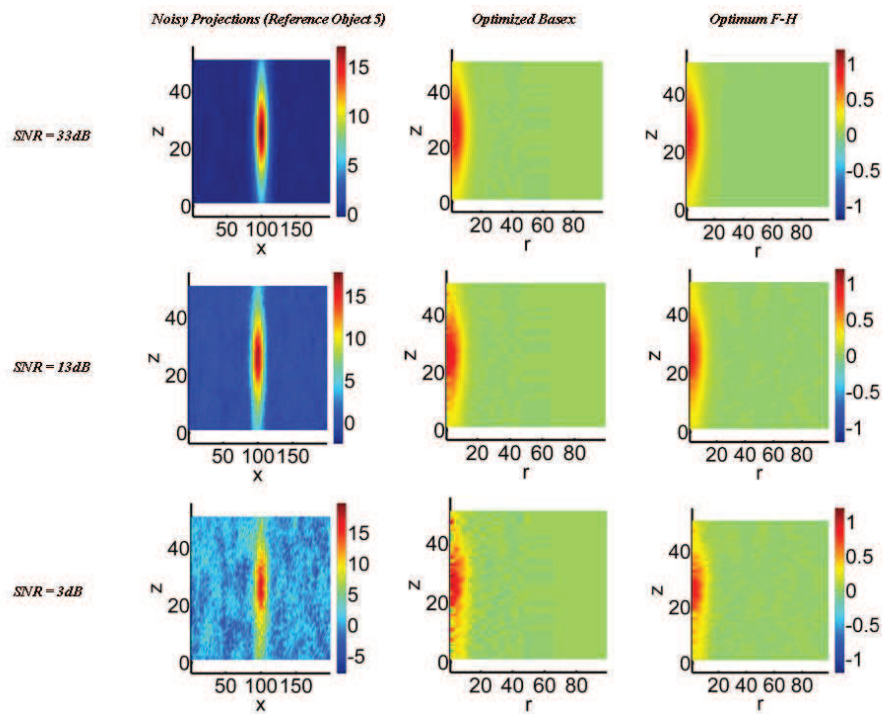




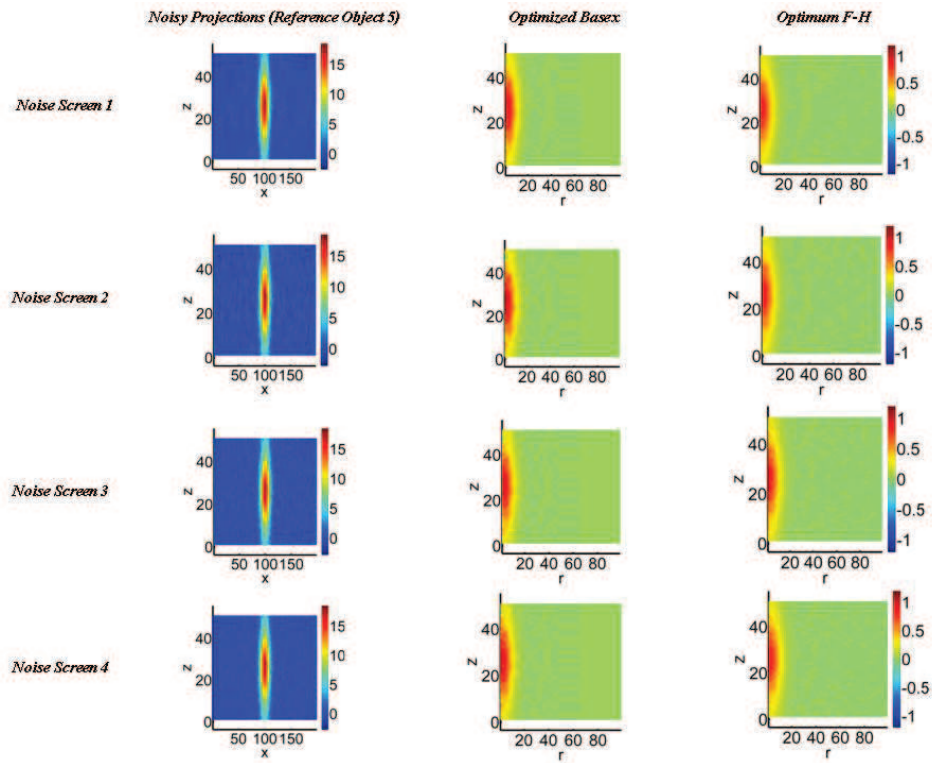
11.



12.



### 13.





1  
2  
3  
4  
5  
6  
7  
8  
9  
10  
11  
12  
13  
14  
15  
16  
17  
18  
19  
20  
21  
22  
23  
24  
25  
26  
27  
28  
29  
30  
31  
32  
33  
34  
35  
36  
37  
38  
39  
40  
41  
42  
43  
44  
45  
46  
47  
48  
49  
50  
51  
52  
53  
54  
55  
56  
57  
58  
59  
60  
61  
62  
63  
64  
65